Regulation of the Micromechanical Properties of Pulmonary Endothelium by S1P and Thrombin: Role of Cortactin

Fernando Terán Arce, Jenny L. Whitlock, Anna A. Birukova, Konstantin G. Birukov, Morton F. Arnsdorf, Ratnesh Lal, Joe G. N. Garcia, and Steven M. Dudek
Department of Medicine, University of Chicago, Chicago, Illinois 60637

ABSTRACT   Disruption of pulmonary endothelial cell (EC) barrier function is a critical pathophysiologic event in highly morbid inflammatory conditions such as sepsis and acute respiratory disease stress syndrome. Actin cytoskeleton, an essential regulator of endothelial permeability, is a dynamic structure whose stimuli-induced rearrangement is linked to barrier modulation. Here, we used atomic force microscopy to characterize structural and mechanical changes in the F-actin cytoskeleton of cultured human pulmonary artery EC in response to both barrier-enhancing (induced by sphingosine 1-phosphate (S1P)) and barrier-disrupting (induced by thrombin) conditions. Atomic force microscopy elasticity measurements show differential effects: for the barrier protecting molecule S1P, the elastic modulus was elevated significantly on the periphery; for the barrier-disrupting molecule thrombin, on the other hand, it was elevated significantly in the central region of the cell. The force and elasticity maps correlate with F-actin rearrangements as identified by immunofluorescence analysis. Significantly, reduced expression (via siRNA) of cortactin, an actin-binding protein essential to EC barrier regulation, resulted in a shift in the S1P-mediated elasticity pattern to more closely resemble control, unstimulated endothelium.

INTRODUCTION

The pulmonary endothelium functions as a semipermeable barrier separating vascular contents from the interstitium and airspaces of the lung (1). Increased endothelial permeability to circulating fluid, proteins, and cells is a characteristic pathophysiologic feature of many inflammatory conditions and often results in pulmonary edema and respiratory failure (2). Endothelial cell (EC) actin cytoskeleton plays a critical role in dynamically regulating the vascular barrier in response to multiple stimuli as well as during other cellular processes such as cell division or migration (1,3). Agonist-induced actin rearrangements result in EC shape changes and altered cell-cell and cell-matrix linkages that combine to modulate barrier function (4). However, the change in cell mechanics caused by the actin rearrangement as well as the effects of the altered mechanical properties on altered EC permeability remain poorly defined.

Atomic force microscopy (AFM) permits the acquisition of structural and elasticity data (5–8) that could be used to define the relation between cell mechanics and cytoskeletal reorganization as a consequence of physiological stimuli (8–12). For example, AFM studies were able to demonstrate that disruption of the cytoskeleton with actin-disrupting agents results in decreased mechanical strength and loss of structural integrity in various cell types, including mammary epithelial cells, fibroblasts, and bovine pulmonary artery EC (10–12).

In this study, we examined cell micromechanical properties in response to barrier-modulating stimuli. We used AFM to mechanically characterize the effects of F-actin cytoskeleton rearrangement mediating permeability changes in cultured human pulmonary artery EC (HPAEC). The permeability change is commonly linked to the barrier-enhancing and barrier-disrupting properties. Here, we used sphingosine 1-phosphate (S1P), a biologically active phospholipid generated by hydrolysis of membrane lipids in activated platelets and other cells that produces significant EC barrier enhancement by means of peripheral actin rearrangement and ligand-receptor binding, strengthening both intercellular and cell–matrix adherence (4,13). We also used thrombin, which acts as a barrier-disrupting agonist causing immediate and profound EC barrier impairment, actin stress fiber formation, and paracellular gap formation (1). We measured differential changes in the local elastic modulus of HPAEC after stimulation with S1P, thrombin, and cortactin. S1P-induced elasticity changes are related to the expression of cortactin, an actin-binding protein with multiple functional domains (14), and is shown to participate in S1P-induced barrier enhancement (15). Our results describe a functional link among actin network organization, micromechanical properties, and endothelial permeability.

MATERIALS AND METHODS

Reagents

Unless otherwise specified, reagents (including S1P and thrombin) were obtained from Sigma (St. Louis, MO). Mouse anticortactin antibody (4F11) was obtained from Upstate Biotechnology (Lake Placid, NY).

Cell culture

HPAEC obtained from Clonetics (Walkersville, MD) were cultured as previously described in EBM-2 complete medium (Clonetics) at 37°C in a humidified atmosphere of 5%CO_2/95% air, with passages 6–10 used for experimentation (15).

Cortactin siRNA treatment

Small interfering RNA (siRNA) targeting human cortactin was obtained as a pool of four siRNA duplexes from Dharmacon (Lafayette, CO) (catalog No. L-010508-00, accession No. NM_005231, NM_138565). Control siRNA (siCONTROL) used was targeting a nonhuman protein, luciferase. EC were treated with siRNA 3 h postseeding, where siRNA were premixed with transfection reagent for 30 min and then diluted with low-serum medium for a final concentration of 50–100 nM siRNA and 6 μl/ml siPORT Amine (Ambion, Austin, TX). After 24 h, an equal volume of serum medium was added to the cells containing siRNA. Silenced cells were used 3–5 days posttransfection, and the medium was replaced a day before all experiments.

Transendothelial monolayer electrical resistance

EC were grown to confluence in polycarbonate wells containing evaporated gold microelectrodes, and transendothelial monolayer electrical resistance (TER) measurements were then performed using an electrical cell-substrate impedance sensing system (Applied Biophysics, Troy, NY) as previously described in detail (13).

Endothelial immunofluorescent imaging

HPAEC were grown on gelatinized coverslips before exposure to various conditions as described for individual experiments. EC were then fixed in 3.7% formaldehyde, permeabilized with 0.25% Triton X-100 for 5 min, washed in phosphate-buffered saline (PBS), blocked with 2% bovine serum albumin in PBS for 30 min, and then incubated for 60 min at room temperature with primary antibody (anticortactin). After washing, EC were then incubated with secondary antibody conjugated to Alexa-488 (or Texas red-conjugated phalloidin for actin staining) for 60 min at room temperature. After further washing with PBS, coverslips were mounted using Slow Fade (Molecular Probes, Eugene, OR) and analyzed using a Nikon Eclipse TE 300 microscope and Sony Digital Photo camera DKC 5000. Images were recorded and saved in Adobe Photoshop.

AFM imaging

All measurements were carried out either with a Bioscope AFM (a prototype of Digital Instruments Bioscope) integrated with a Zeiss Axiovert 135TV inverted light microscope, using the NanoScope III software (Version 5,12R3) or with a Nanoscope III Extended Multimode AFM from Veeco (Santa Barbara, CA) using a 150×150 μm^2 ''J'' scanner. To fix HPAEC for AFM imaging, the cells were first rinsed with 2 ml of 10 mM PBS, pH 7.4 containing 0.5 mM $CaCl_2$ and 2 mM glutamine. Next, the cells were fixed using 2 ml of 0.5% glutaraldehyde final concentration from a stock solution of 50% (Sigma-Aldrich, St. Louis, MO) for 5 min, followed by washing three times with water, ACS grade (Sigma-Aldrich). The coverslips were then left to air dry. Imaging of glutaraldehyde-fixed cells was performed in PBS buffer using contact mode. Cantilevers with nominal spring constants of $k =$ 0.06 N/m purchased from Veeco were utilized for imaging and elasticity measurements. The same cantilever was used to compare mechanical properties of control cells and S1P- and thrombin-treated cells. Cantilever spring constants were measured using standard calibrated cantilevers (CLFC-NOBO, Veeco) (16,17). The tip radius was determined using gold colloidal nanoparticles (Ted Pella, Redding, CA) (18).

Mechanical properties were measured by acquiring point-by-point force versus distance curves over 32×32 and 64×64 arrays (force-volume) (9,12). For each point in the array, a force curve can be recalled, from which physical properties, such as the elasticity, can be derived quantitatively. At each point of the array of force versus distance curves, the piezo continuously moves the sample toward the tip until a threshold cantilever deflection is reached. The position of the piezo at the deflection threshold determines the height of the sample at each point of the array. The collection of these data points generates the height image. A force-volume image is formed by plotting the cantilever deflection at a given piezo position for each of the approach or retraction curves. The tip velocities for these measurements varied between 1 μm/s and 3 μm/s. The sensitivity of the photodetector was calibrated by acquiring force versus distance curves on a clean glass substrate.

Data analysis

Large-scale AFM images (Fig. 1, *A* and *B*) were acquired to ensure that the analyzed cells displayed characteristic features compatible with fluorescence images. In this region, an individual cell was selected for further imaging and elasticity measurements. A home-written MATLAB (The MathWorks, Natick, MA) code was used to obtain elasticity maps (Fig. 1 *C*) from force-volume data (19). The cell's periphery and nucleus in the elasticity map (Fig. 1 *D*) were defined from AFM height images acquired in contact mode. Our program allowed data points to be selected in the associated height image from the force volume file and their indices to be transferred to the elasticity map for analysis. Dozens to hundreds of data points inside each region were selected by choosing the start and end points of polygonal segments. These segments were then connected together to find the elastic moduli in the cell's nucleus and peripheral region. If only two points were selected, the program delivered a cross section of the selected line. To obtain ratios of elastic moduli at the peripheral and central regions of cells, average values and standard errors of all data points inside each region were calculated. These values were subsequently used to determine the elasticity ratio. To obtain elasticity maps, force versus distance curves (Fig. 1 *E*) were transformed into indentation curves (Fig. 1 *F*), and subsequently these were fitted according to the Hertzian model to obtain the values of the elastic modulus plotted in the maps (9,12,20–24). To measure the heights of cells (Table 1), the grain size analysis option in the nanoscope software was utilized.

To obtain indentation curves, a line of zero force was defined from the average deflection of the points in the force curve that correspond to the positions of the cantilever far away from the surface. The number of these points depended on the force-volume data set. The origin of the indentation curve was chosen as the point where the retraction curve intersected the line of zero force. The cell's vertical deformation (penetration depth of the tip) was obtained by subtracting the cantilever deflection from the displacement of the piezo. These values were plotted along the *x* axis of the indentation curve. Forces were calculated by multiplying the elastic constant of the cantilever by the cantilever deflection. To check the consistency of these results, a manual one-by-one analysis of a representative subset of force curves was performed, and, if necessary, the data were reanalyzed until the computed and manual results agreed. When the sample was either too thin (<200 nm) or absent in a region of the image, the elastic modulus exceeded the values found typically in the analysis. Consequently, a value of 0 was assigned to the elastic modulus in that region, and it was excluded from further analysis. The same procedure was followed for data points that exceeded typical values, regardless of the specimen's thickness in the region. The threshold value was usually between 1 MPa and 2.5 MPa.

RESULTS AND DISCUSSION

To first characterize our AFM analysis relative to established cultured EC light microscopy, parallel dishes of HPAEC
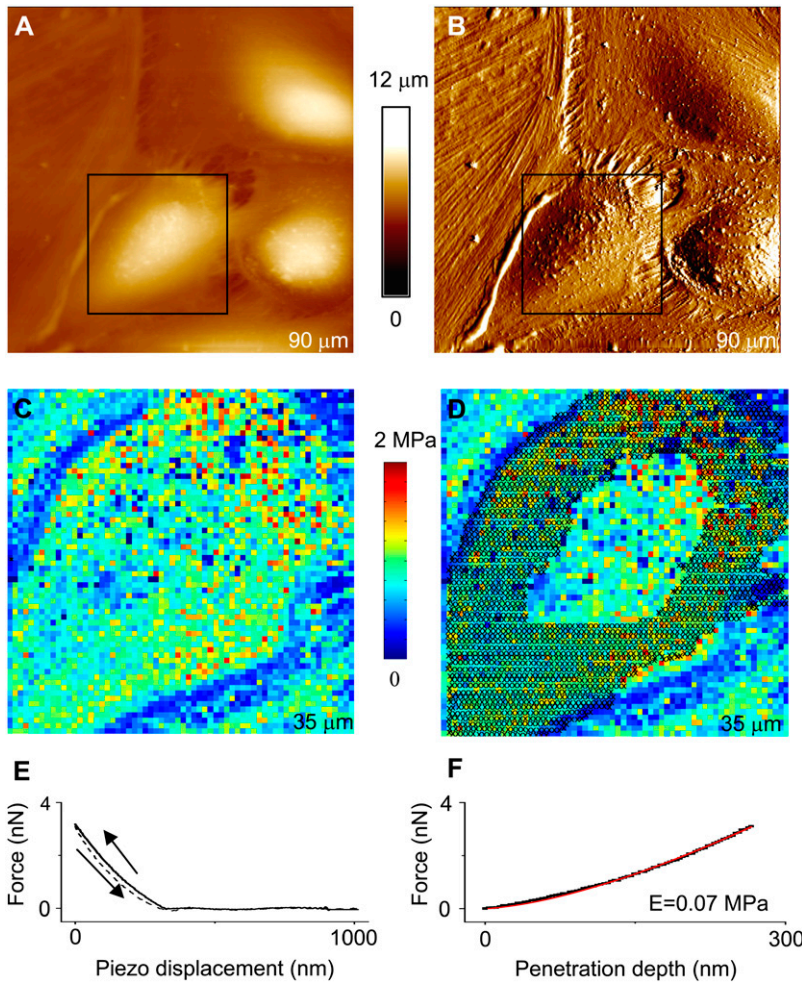
FIGURE 1 Correlation between elasticity and morphology for human pulmonary EC. AFM images, (*A*) height and (*B*) deflection, showing the morphology of human pulmonary EC grown to confluence. Network of actin fibers and cell processes are visible, particularly in the deflection image. Elasticity maps (*C*) were obtained to find the ratio, E_C/E_n, between elastic moduli at the cell periphery (E_C) and cell nucleus (E_n). (*D*) The crosses in the elasticity map indicate the peripheral region of the analyzed cell, and the nucleus region is enclosed. Subsequently, the average value of all data points inside each region was determined to find E_C/E_n. In this particular case, a value $E_C/E_n = 1.05 \pm 0.02$ was found. Elasticity maps were obtained by transforming (*E*) force versus distance curves into (*F*) indentation curves and fitting the approach portion of the curves (*black solid lines*) with the Hertz model (*red solid lines*). The retraction curve (*E*) is displayed with dashed lines. At forces used during contact mode imaging ($\sim$1 nN), the cell deformation (penetration depth of the tip) was typically between 50 nm and 200 nm.

were grown to confluence, stimulated with vehicle, S1P, or thrombin for 5 min, and then fixed and analyzed as shown in Fig. 2. Light microscopy with standard immunofluorescence for F-actin revealed a fairly disorganized pattern in vehicle-

**TABLE 1 Summary of E_C/E_n ratios and heights for all analyzed cells**

Treatment	H_n (nm)	H_C (nm)	E_C/E_n
Control	3152 ± 179	2284 ± 91	0.81 ± 0.01
Thrombin	4079 ± 901	2770 ± 278	0.61 ± 0.12*
S1P	2965 ± 81	2163 ± 99	1.11 ± 0.08*

H_C refers to the maximum height in the cell's cytoplasm. Heights above this value correspond to the cell's nucleus. H_n indicates the maximum height of the cell's nucleus and therefore of the entire cell. Heights were measured for five different cells in the case of control and S1P-treated cells, but only four cells were analyzed in the case of thrombin (4). The E_C/E_n ratios provided in the table are values obtained after taking the ratio of the combined average results from four different cells of each sample. The number of data points analyzed in the regions corresponding to the cell's nucleus and cytoplasm, N_C and N_n, from which these ratios were obtained are $N_C = 487$ and $N_n = 199$ for control cells, $N_C = 2821$ and $N_n = 392$ for thrombin-treated cells, and $N_C = 2692$ and $N_n = 380$ for S1P-treated cells. Quantities represent average values ± standard errors of the mean.
*After Anova testing, E_C/E_n are statistically significantly different for S1P and thrombin treatments ($p = 0.02$).

treated EC (Fig. 2 *D*), whereas stimulation with either S1P or thrombin produced rapid reorganization of actin filaments. The potent EC barrier-enhancing agent, S1P, induced a substantial increase in peripheral F-actin (indicated by *small arrows* in Fig. 2 *E*) as previously described (13), whereas the barrier-disrupting agent thrombin induced transcellular stress fiber formation (*small arrows* in Fig. 2 *F*) (1). These differential effects on F-actin distribution are consistent with our previous observations and reflect cytoskeletal patterns associated with permeability changes in cultured EC. Thrombin-induced stress fiber formation results in a well-characterized sequence of events including increased actomyosin interaction, cellular contraction along these cables, subsequent intercellular gap formation (*arrows* in Fig. 2, *C*, *F*, and *I*), and increased permeability. In contrast, even though increased peripheral F-actin has been observed in association with multiple barrier-enhancing stimuli including S1P, shear stress, HGF (hepatocyte growth factor), ATP, and simvastatin (13,25–28), the mechanistic translation of this cytoskeletal rearrangement into the functional effect of decreased permeability remains poorly defined.

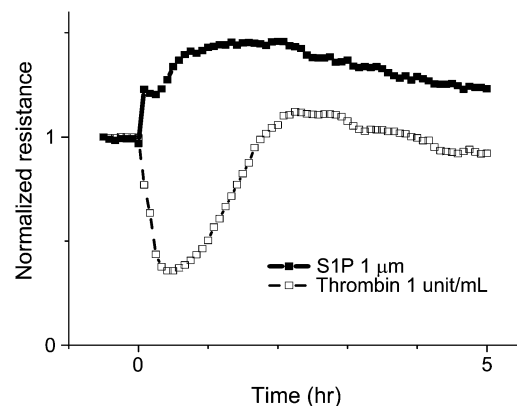S1P and thrombin also induced differential cellular localization of the actin-binding protein, cortactin (Fig. 2, *G–I*).
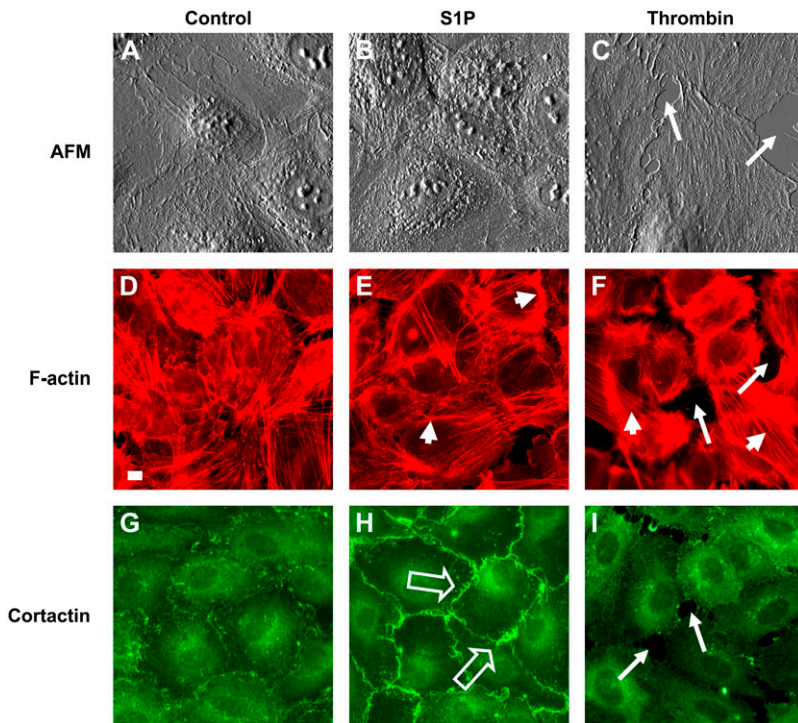
FIGURE 2   S1P and thrombin induce differential effects on EC cytoskeletal structure. Cultured HPAEC were treated with vehicle (control: images *A*, *D*, and *G*), S1P (1 μM: images *B*, *E*, and *H*), or thrombin (1 unit/ml: images *C*, *F*, and *I*) for 5 min and then fixed as described in Materials and Methods. Separate samples were then analyzed by AFM (*top row*; images *A*, *B*, and *C*) or standard immunofluorescence for F-actin (*middle row*; images *D*, *E*, and *F*) and cortactin (*bottom row*; images *G, H*, and *I*) distribution. Vehicle-treated EC exhibited disorganized F-actin staining and scattered peripheral and cytoplasmic cortactin staining (*D* and *G*), whereas S1P induced peripheral F-actin (*small arrows*, *E*) and cortactin redistribution (*open arrows*, *H*) as previously described (15). In contrast, thrombin produced intercellular gap formation (*arrows*, *F* and *I*), F-actin stress fiber formation (*small arrows*, *F*), and loss of peripheral cortactin staining (*I*). All AFM images are displayed in deflection mode and have a size of $80 \times 80 \ \mu m^2$. The scale, displayed as white bar in F-actin control image = 10 μm, is the same for all fluorescence images.

We have previously reported that cortactin, a multidomain protein that both stimulates peripheral actin polymerization (via its interaction with the Arp2/3 complex) as well as crosslinks and stabilizes these actin filaments after formation (14), plays an integral role in S1P- and ATP-induced EC barrier enhancement (15,27). In our current study, light microscopy with standard immunofluorescence revealed scattered peripheral and cytoplasmic cortactin staining in vehicle-treated cells (Fig. 2 *G*), whereas S1P rapidly induced redistribution of cortactin to the EC periphery as previously described (Fig. 2 *H*) (15). In contrast, the barrier-disrupting agent thrombin produced a loss of peripheral cortactin staining (Fig. 2 *I*). These cytoskeletal changes were associated with altered HPAEC barrier function as measured by TER, a highly sensitive measure of permeability, with S1P and thrombin rapidly increasing or decreasing barrier function, respectively (Fig. 3).

We then characterized these permeability states via AFM. HPAEC were grown to confluence, fixed, and imaged in PBS buffer. EC were first imaged using contact mode, and then force-volume data were collected immediately thereafter. AFM images of untreated cells used as control (Fig. 4, *A–C*) as well as of cells treated either with the barrier-disrupting agonist thrombin (Fig. 4, *D–F*) or with the barrier-enhancing antagonist S1P (Fig. 4, *G–I*) showed an overall cell morphology consistent with features observed in light microscopy (Fig. 2, *D–I*). For the control cells, the measured height of the cell nucleus was $\sim$2.5 μm, and the cytoplasmic region had a height of $\sim$650 nm (Fig. 4 *B*). Elasticity maps (Fig. 4, *C*, *F*, and *I*) revealed inhomogeneities in the elasticity maps

of cells, which correlated with their morphological features. For untreated cells (Fig. 4 *C*), the elastic modulus on the cell's nucleus (E_n) was generally comparable to, or somewhat higher than, the elastic modulus measured in the peripheral cytoplasmic region (E_c). Values of E_c/E_n were generally

FIGURE 3   S1P and thrombin induce differential effects on EC barrier function. HPAEC were plated in monolayer on gold microelectrodes and grown to confluence to measure TER as described in Materials and Methods. After 30 min of baseline measurements, S1P (1 μM) or thrombin (1 unit/ml) were added at time 0 to individual wells. S1P (*solid squares*, *solid line*) induced rapid and sustained increased barrier function (indicated by increased resistance across the EC monolayer), whereas thrombin (*open squares*, *dashed line*) rapidly and potently decreased EC barrier function (indicated by decreased resistance). Representative TER tracings normalized to starting resistances are shown. Experiments were independently performed dozens of times and are consistent with previously published results (13).
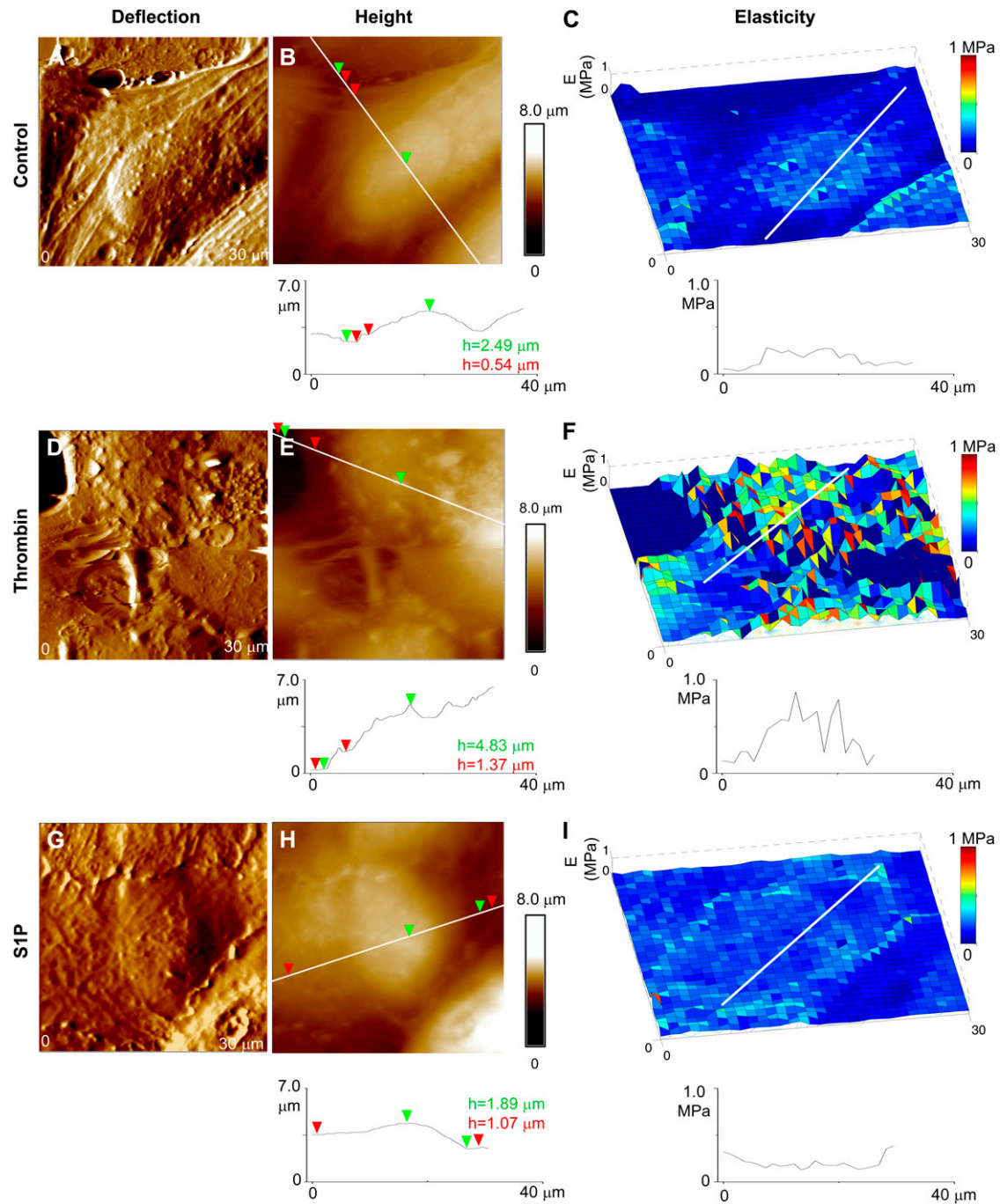
FIGURE 4   Elasticity changes in human pulmonary EC induced by barrier-disrupting (thrombin) and barrier-enhancing agents (S1P). Deflection and height AFM images are displayed alongside elasticity maps for comparison between morphological and mechanical properties. (A–C) Untreated cells used as control, (D–F) cells treated with thrombin and (G–I) cells treated with S1P. Data were acquired using the same cantilever with 0.06 N/m spring constant in PBS buffer at room temperature, as described in Materials and Methods.

0.5–1. Values of the cell's elastic modulus were typically in the 0.1–1 MPa range, in agreement with previous work that studied the effect of glutaraldehyde fixation on the elastic modulus of mouse fibroblasts and the RDX2C2 cell line (29). For the maximum loads applied during our experiments (∼5 nN), deformation of the HPAEC under the AFM tip was typically ∼200 nm. For comparison with the just described results obtained in PBS medium, similar measurements were carried out in air with dried cells, resulting in a flattening of cells and an increase of ∼3 orders of magnitude in the measured values of the elastic modulus, which is attributed to dehydration effects.
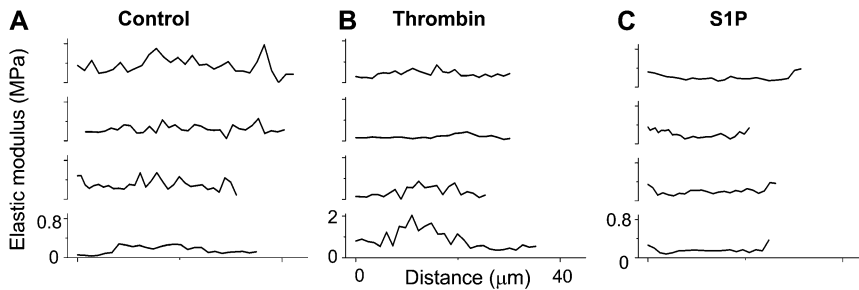
FIGURE 5 Differential effects of S1P and thrombin on distribution of endothelial elasticity. (*A–C*) Cross sections for multiple cells (four per condition) illustrating differences in elasticity at the cell's periphery (edges) and nucleus (central region) for (*A*) control, (*B*) thrombin-treated, and (*C*) S1P-treated cells. The scale in the *x* axis is common to all panels. In each panel, the *y* axis is the same for all cross sections.

Changes in cell morphology and elasticity in response to thrombin and S1P treatments were imaged. The change in the overall elastic modulus as a result of agonist/antagonist action is complicated by several effects, including sample preparation and AFM measurement technique. Among effects caused by the sample itself, variability in mechanical properties among individual cells, possibly because of different stages of growth of individual cells inside a given cell population and effects from cell fixation can be mentioned (30). On the other hand, variability in tip radius and spring constant among cantilevers used for AFM indentation measurements, even after appropriate calibration has been performed, also affect a fair comparison of mechanical properties. Furthermore, experiments with live HPAEC are complicated by poor cell adhesion and the rapid action of agonist/antagonist agents in timescales difficult to follow with the AFM. Therefore, for these initial experiments, relative variations in the elastic modulus of the peripheral cytoplasm to the elastic modulus in the cell nucleus were studied using fixed cells, and these results were compared with the results using techniques mentioned in the previous sections.

Thrombin treatment resulted in an increase in cell height and overall disruption of cell morphology (Fig. 4, *D* and *E*), in accordance with the induced retraction of EC and widening of interendothelial junctions as a result of ''rounding up'' of the cells (31). S1P had the converse effect of ''flattening'' the cells, thus resulting in a decrease of the measured height (Fig. 4, *G* and *H*). For thrombin, the cells' cytoplasm had typical heights of ~1.4 μm, and the cells' nuclei reached values of ~5 μm, often surpassing the vertical range of the AFM-scanner (Fig. 4 *E*), for S1P the heights of the cytoplasm and nucleus were ~1 μm and ~3 μm, respectively (Fig. 4 *H*). Table 1 shows this tendency in more detail. Heights for the cells' nuclei, H_n, are underestimated for the control and in particular for the thrombin-treated cells because only the cells with heights lower than the vertical range of our AFM scanner could be analyzed. Along with this tendency, a minor increase (decrease) in the maximum height, H_C, of the cytoplasmic region is also observed for the thrombin (S1P)-treated cells. Accompanying these morphological changes, an increase in the elastic modulus of the nucleus region with respect to the peripheral cytoplasmic region was observed for the thrombin-treated cells (Fig. 4 *F*). E_c/E_n ratios for EC decreased to values of 0.25–0.5 after this treatment. In contrast, S1P treatment increased the modulus of the cytoplasmic region relative to the nucleus region while slightly decreasing the overall elastic modulus of the cell (Fig. 4 *F*). Typically, E_c/E_n ratios increased to ~1.0–1.25, but sometimes higher,
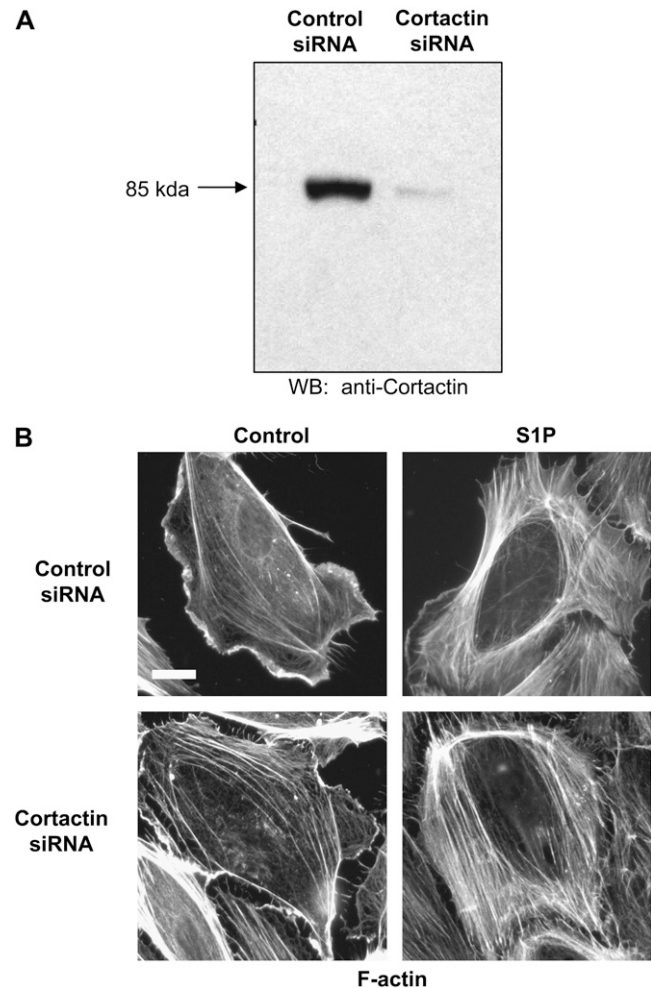

FIGURE 6 Depletion of cortactin protein expression does not attenuate S1P-induced cortical F-actin rearrangement. HPAEC were treated with control or cortactin siRNA as described in Materials and Methods. (*A*) Western blot of whole-cell lysates demonstrated depletion of cortactin protein expression by ~90% in the cortactin siRNA-treated EC. (*B*) Control and cortactin siRNA-treated HPAEC were stimulated with vehicle (control) or S1P (1 μM) for 5 min and then fixed and immunostained for F-actin. S1P rapidly induced a dramatic increase in peripheral F-actin in both types of siRNA-treated EC. Scale for all images: white bar in Control siRNA control image = 10 μm.

and were statistically different from ratios measured in thrombin-treated cells when data from multiple cells were averaged (Table 1).

The differential effects of S1P compared to thrombin and vehicle treatment on the spatial distribution of EC elastic properties are illustrated in Fig. 5, which represents cross sections for four different cells after each treatment. In these graphs, the x axis represents the distance across the cell where the nucleus was chosen as the central region in the plot and the sides were chosen in the cytoplasmic peripheral region (as represented in Fig. 4, *C*, *F*, and *I*), whereas the y axis denotes the elastic modulus range. Both control and thrombin-stimulated EC show higher elastic modulus in the center of the cells, but for the thrombin-stimulated EC this was more pronounced (note the difference in scale for the elastic modulus in the thrombin compared with control or S1P graphs). This differential effect likely represents the effects of increased transcellular actin stress fibers shown previously (Fig. 2 *F*). In contrast, S1P treatment induced a flattening in the central portion of the cells, and the highest elastic moduli occurred at the EC periphery in correlation with the enhanced

peripheral actin and cortactin observed by light microscopy (Fig. 2 *E*). Table 1 summarizes the results of E_c/E_n ratios for the different analyzed cells.

As described above, cortactin concentrates at the cell periphery after S1P stimulation, where it appears to participate in cytoskeletal rearrangements necessary for increased EC barrier function because suppression of cortactin protein expression inhibits S1P-induced TER elevations (15). To determine the effect of cortactin expression on EC elasticity distribution, we utilized siRNA to specifically deplete cortactin protein levels by $\sim$90% (Fig. 6 *A*). Interestingly, the HPAEC were still able to exhibit increased peripheral F-actin concentration in response to S1P despite this level of cortactin depletion (Fig. 6 *B*). We next measured the elasticity of S1P-stimulated EC in which cortactin expression was suppressed by siRNA and compared that with EC treated with control siRNA (Fig. 7). Significantly, in the cortactin-depleted EC, S1P stimulation resulted in an elastic modulus on the periphery relatively decreased compared to the more central elastic modulus surrounding the nucleus (Fig. 7 *C*), with $E_c/E_n \approx 0.3$–0.9. In fact, these values are
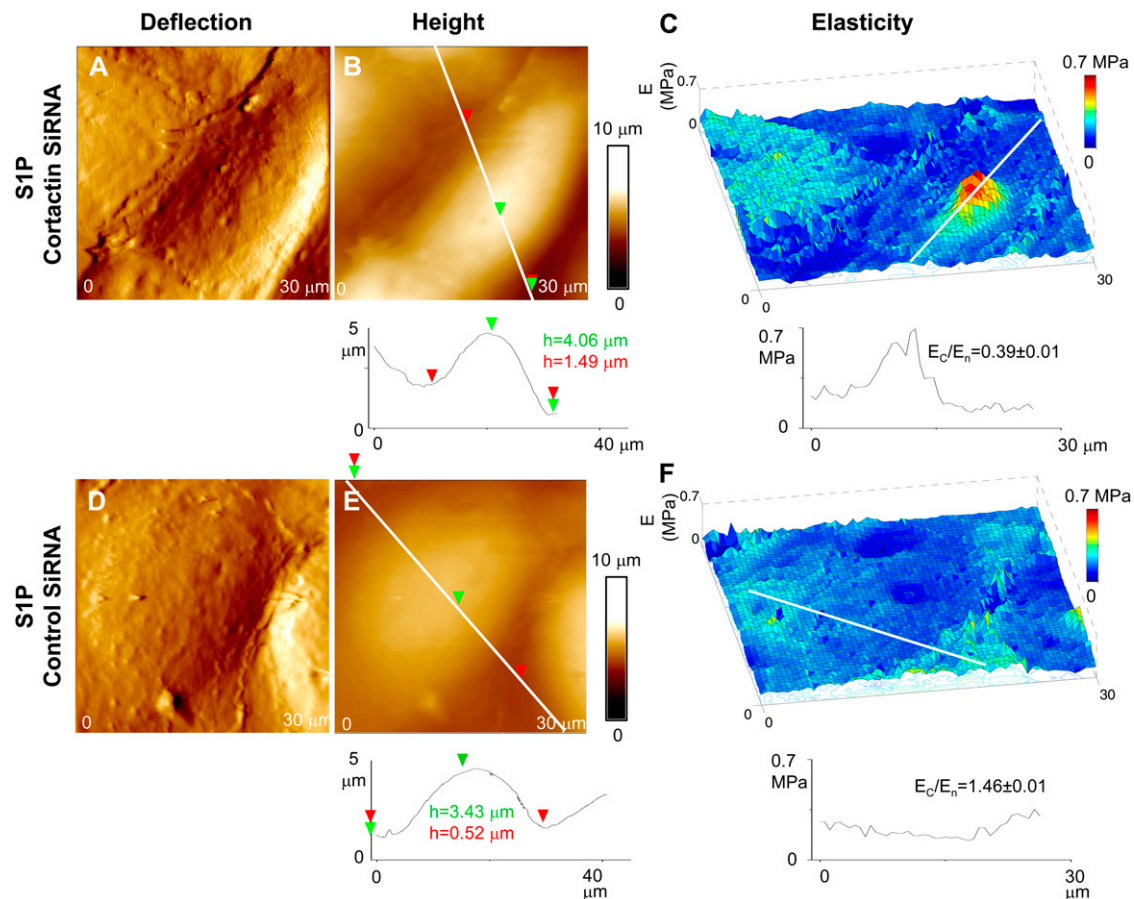

FIGURE 7   Depletion of cortactin alters morphology and elastic properties for S1P-stimulated cells. (*A–C*) Cortactin levels were depleted using cortactin-SiRNA, and (*D–F*) cells were treated with control-SiRNA; thus, cortactin levels were not suppressed. (*C*) The elastic modulus at the cells periphery, E_c, decreased noticeably with respect to that at the cell's nucleus, E_n, for EC having depleted cortactin content, but (*F*) E_c remained slightly increased compared to E_n for cells treated with control RNA. Shown is a representative sample of multiple analyzed cells.

most similar to those measured for the unstimulated control cells described in Fig. 4, Fig. 5, and Table 1. However, in cells treated with control siRNA (in which cortactin expression was not suppressed), the elastic modulus at the cell's periphery increased in relation to the elastic modulus around the nucleus after S1P stimulation. $E_c/E_n \approx 1.1$–1.7 was found in this case, in agreement with other sets of experiments for S1P-treated cells (Fig. 4, Fig. 5, and Table 1). Thus, depletion in cortactin protein levels prevented the redistribution of elasticity to the EC periphery induced by S1P, indicating an important role for this actin-binding protein in mediating EC structural changes associated with enhanced barrier function.

CONCLUSION

In summary, the differential effects of S1P-induced barrier enhancement and thrombin-induced barrier disruption on the distribution of the cytoskeletal proteins F-actin and cortactin correlate with differential elasticity measurements by AFM. S1P rapidly increases EC TER in association with a peripheral distribution of F-actin, cortactin, and elasticity, whereas thrombin decreases TER as actin stress fibers and elasticity concentrate in the midportions of the cell. Moreover, novel functional insights into the role of cortactin in mediating S1P-induced barrier enhancement (15) are provided by siRNA depletion of its protein expression. Although S1P still induces strong peripheral F-actin accumulation in cortactin-deficient EC (Fig. 6 B), the elastic modulus of these cells resembles that of unstimulated control cells. These data suggest that one important function of cortactin in S1P-induced barrier enhancement may be to crosslink and stabilize peripheral F-actin fibers to mechanically promote increased EC barrier function. Further study using similar approaches would broaden our understanding of the mechanistic regulation of vascular permeability and perhaps lead to the clinically important goal of effective modulation of this barrier function.

REFERENCES

1. Dudek, S. M., and J. G. N. Garcia. 2001. Cytoskeletal regulation of pulmonary vascular permeability. *J. Appl. Physiol.* 91:1487–1500.

2. Jacobson, J. R., and J. G. Garcia. 2007. Novel therapies for microvascular permeability in sepsis. *Curr. Drug Targets.* 8:509–514.

3. Lee, J. S., and A. I. Gotlieb. 2003. Understanding the role of the cytoskeleton in the complex regulation of the endothelial repair. *Histol. Histopathol.* 18:879–887.

4. McVerry, B. J., and J. G. N. Garcia. 2005. In vitro and in vivo modulation of vascular barrier integrity by sphingosine 1-phosphate: mechanistic insights. *Cell. Signal.* 17:131–139.

5. Arnsdorf, M. F., and S. Xu. 1996. Atomic (scanning) force microscopy in cardiovascular research. *J. Cardiovasc. Electrophysiol.* 7:639–652.

6. El Kirat, K., I. Burton, V. Dupres, and Y. F. Dufrene. 2005. Sample preparation procedures for biological atomic force microscopy. *J. Microsc.* 218:199–207.

7. Lal, R., and S. A. John. 1994. Biological applications of atomic-force microscopy. *Am. J. Physiol.* 266:C1–C21.

8. Shroff, S. G., D. R. Saner, and R. Lal. 1995. Dynamic micromechanical properties of cultured rat atrial myocytes measured by atomic-force microscopy. *Am. J. Physiol. Cell Physiol.* 38:C286–C292.

9. Almqvist, N., R. Bhatia, G. Primbs, N. Desai, S. Banerjee, and R. Lal. 2004. Elasticity and adhesion force mapping reveals real-time clustering of growth factor receptors and associated changes in local cellular rheological properties. *Biophys. J.* 86:1753–1762.

10. Pesen, D., and J. H. Hoh. 2005. Micromechanical architecture of the endothelial cell cortex. *Biophys. J.* 88:670–679.

11. Rotsch, C., and M. Radmacher. 2000. Drug-induced changes of cytoskeletal structure and mechanics in fibroblasts: An atomic force microscopy study. *Biophys. J.* 78:520–535.

12. Quist, A. P., S. K. Rhee, H. Lin, and R. Lal. 2000. Physiological role of gap-junctional hemichannels: Extracellular calcium-dependent isosmotic volume regulation. *J. Cell Biol.* 148:1063–1074.

13. Garcia, J. G., F. Liu, A. D. Verin, A. Birukova, M. A. Dechert, W. T. Gerthoffer, J. R. Bamberg, and D. English. 2001. Sphingosine 1-phosphate promotes endothelial cell barrier integrity by Edg-dependent cytoskeletal rearrangement. *J. Clin. Invest.* 108:689–701.

14. Cosen-Binker, L. I., and A. Kapus. 2006. Cortactin: the gray eminence of the cytoskeleton. *Physiology (Bethesda).* 21:352–361.

15. Dudek, S. M., J. R. Jacobson, E. T. Chiang, K. G. Birukov, P. Y. Wang, X. Zhan, and J. G. N. Garcia. 2004. Pulmonary endothelial cell barrier enhancement by sphingosine 1-phosphate—roles for cortactin and myosin light chain kinase. *J. Biol. Chem.* 279:24692–24700.

16. Serre, C., P. Gorostiza, A. Perez-Rodriguez, F. Sanz, and J. R. Morante. 1998. Measurement of micromechanical properties of polysilicon microstructures with an atomic force microscope. *Sens. Actuators A Phys.* 67:215–219.

17. Tortonese, M., and M. Kirk. 1997. Characterization of application specific probes for SPMs. Proceedings of SPIE-The International Society for Optical Engineering 3009 (Micromachining and Imaging). 53–60.

18. Vesenka, J., S. Manne, R. Giberson, T. Marsch, and E. Henderson. 1993. Colloidal gold particles as an incompressible atomic-force microscope imaging standard for assessing the compressibility of biomolecules. *Biophys. J.* 65:992–997.

19. Arce, F. T., R. Avci, I. B. Beech, K. E. Cooksey, and B. Wigglesworth-Cooksey. 2006. Modification of surface properties of a poly(dimethyl-siloxane)-based elastomer, RTV11, upon exposure to seawater. *Langmuir.* 22:7217–7225.

20. Arce, F. T., R. Avci, I. B. Beech, K. E. Cooksey, and B. Wigglesworth-Cooksey. 2003. Microelastic properties of minimally adhesive surfaces: A comparative study of RTV11™ and Intersleek elastomers™. *J. Chem. Phys.* 119:1671–1682.

21. Arce, P. F. M. T., G. A. Riera, P. Gorostiza, and F. Sanz. 2000. Atomic-layer expulsion in nanoindentations on an ionic single crystal. *Appl. Phys. Lett.* 77:839–841.

22. Hues, S. M., and C. F. Draper. 1998. Derivation of quantitative mechanical properties. *In* Procedures in Scanning Probe Microscopies. R. J. Colton, A. Engel, J. E. Frommer, H. E. Gaub, A. Gewirth, R. Guckenberger, J. Rabe, W. M. Heckl, and B. Parkinson editors. John Wiley & Sons, Chichester, UK.

23. Johnson, K. L. 1985. Contact Mechanics. Cambridge University Press, Cambridge, UK.

24. Sneddon, I. N. 1965. The relation between load and penetration in the axisymmetric Boussinesq problem for a punch of arbitrary profile. *Int. J. Eng. Sci.* 3:47–57.

25. Birukov, K. G., A. A. Birukova, S. M. Dudek, A. D. Verin, M. T. Crow, X. Zhan, N. DePaola, and J. G. N. Garcia. 2002. Shear stress-mediated cytoskeletal remodeling and cortactin translocation in pulmonary endothelial cells. *Am. J. Respir. Cell Mol. Biol.* 26:453–464.

26. Jacobson, J. R., S. M. Dudek, K. G. Birukov, S. Q. Ye, D. N. Grigoryev, R. E. Girgis, and J. G. N. Garcia. 2004. Cytoskeletal activation and altered gene expression in endothelial barrier regulation by simvastatin. *Am. J. Respir. Cell Mol. Biol.* 30:662–670.

27. Jacobson, J. R., S. M. Dudek, P. A. Singleton, I. A. Kolosova, A. D. Verin, and J. G. N. Garcia. 2006. Endothelial cell barrier enhancement by ATP is mediated by the small GTPase Rac and cortactin. *Am. J. Physiol. Lung Cell. Mol. Physiol.* 291:L289–L295.

28. Liu, F., K. L. Schaphorst, A. D. Verin, K. Jacobs, A. Birukova, R. M. Day, N. Bogatcheva, D. P. Bottaro, and J. G. Garcia. 2002. Hepatocyte growth factor enhances endothelial cell barrier function and cortical cytoskeletal rearrangement: potential role of glycogen synthase kinase-3beta. *FASEB J.* 16:950–962.

29. Hutter, J. L., J. Chen, W. K. Wan, S. Uniyal, M. Leabu, and B. M. C. Chan. 2005. Atomic force microscopy investigation of the dependence of cellular elastic moduli on glutaraldehyde fixation. *J. Microsc.* 219:61–68.

30. Moloney, M., L. McDonnell, and H. O'Shea. 2004. Atomic force microscopy of BHK-21 cells: an investigation of cell fixation techniques. *Ultramicroscopy.* 100:153–161.

31. Tiruppathi, C., A. B. Malik, P. J. Delvecchio, C. R. Keese, and I. Giaever. 1992. Electrical method for detection of endothelial-cell shape change in real-time—assessment of endothelial barrier function. *Proc. Natl. Acad. Sci. USA.* 89:7919–7923.